Linear electromagnetic excitation of an asymmetric low pressure capacitive discharge with unequal sheath widths

M. A. Lieberman, A. J. Lichtenberg, E. Kawamura, and P. Chabert

---

Articles you may be interested in

Energy distribution of electron flux at electrodes in a low pressure capacitively coupled plasma
J. Appl. Phys. **113**, 023306 (2013); 10.1063/1.4774306

Power absorption in electrically asymmetric dual frequency capacitive radio frequency discharges
Phys. Plasmas **18**, 013503 (2011); 10.1063/1.3535542

Fluid modeling of electron heating in low-pressure, high-frequency capacitively coupled plasma discharges
J. Appl. Phys. **96**, 6073 (2004); 10.1063/1.1818354

Synthesis of sheath voltage drops in asymmetric radio-frequency discharges
J. Appl. Phys. **96**, 127 (2004); 10.1063/1.1759787

Stochastic heating in field-reversed low pressure discharges
Phys. Plasmas **7**, 185 (2000); 10.1063/1.873793

Linear electromagnetic excitation of an asymmetric low pressure capacitive discharge with unequal sheath widths

M. A. Lieberman,[1,a)] A. J. Lichtenberg,[1] E. Kawamura,[1] and P. Chabert[2]
[1]*Department of Electrical Engineering and Computer Science, University of California, Berkeley, California 94720-1770, USA*
[2]*Laboratoire de Physique des Plasmas, CNRS, Ecole Polytechnique, UPMC, Paris XI, Observatoire de Paris, 91128 Palaiseau, France*

It is well-known that standing waves having radially center-high radio frequency (rf) voltage profiles exist in high frequency capacitive discharges. In this work, we determine the symmetric and antisymmetric radially propagating waves in a cylindrical capacitive discharge that is asymmetrically driven at the lower electrode by an rf voltage source. The discharge is modeled as a uniform bulk plasma which at lower frequencies has a thicker sheath at the smaller area powered electrode and a thinner sheath at the larger area grounded electrode. These are self-consistently determined at a specified density using the Child law to calculate sheath widths and the electron power balance to calculate the rf voltage. The fields and the system resonant frequencies are determined. The center-to-edge voltage ratio on the powered electrode is calculated versus frequency, and central highs are found near the resonances. The results are compared with simulations in a similar geometry using a two-dimensional hybrid fluid-analytical code, giving mainly a reasonable agreement. The analytic model may be useful for finding good operating frequencies for a given discharge geometry and power. © 2016 AIP Publishing LLC. [http://dx.doi.org/10.1063/1.4938204]

I. INTRODUCTION

Large-area plasma processing systems, capacitively driven at frequencies higher than the conventional frequency of 13.56 MHz, are widely used for silicon wafer and flat panel processing. Large area sources are required as wafer size increases, and higher frequency produces higher ion flux at reduced ion bombarding energy, required to process integrated circuits with smaller critical dimensions. The physics of conventional frequency (13.56 MHz) moderate area capacitive reactors, described within the electrostatics approximation, is reasonably well understood.[1–3] For higher frequencies and larger areas, electromagnetic effects, such as standing waves and skin effects, can limit processing uniformity.[4,5] To understand these effects, discharge models based on the propagation of electromagnetic waves have been developed,[6,7] with the electromagnetics treated in the linearized frequency domain. These models considered uniform electron density in the bulk plasma and fixed sheath size, but linear (in the frequency domain) transmission line models were later coupled to Child law sheaths and to particle and energy balance to obtain more self-consistent radial variations of the wave properties, sheath size, and electron density.[8–12] Numerical simulations in the frequency domain were also used to study the electromagnetic effects self-consistently with the plasma transport in two dimensions.[13–16] Results from the full nonlinear discharge dynamics, in the time-domain, were obtained in more sophisticated numerical simulations,[17–22] but the detailed underlying physics was not explored. The overall conclusion is that, for large area discharges at high frequencies, the shortened

wavelengths can excite significant center-high plasma non-uniformities. We have also explored the effects of nonlinearly generated harmonics for an idealized nonlinear transmission line discharge model.[23] We found that these harmonics generated significant central electron power deposition highs, even at the lowest frequencies investigated.

Both a *z*-symmetric, radially varying standing wave mode[5,6,8,9,24–28] and a *z*-antisymmetric mode can exist in asymmetrically excited capacitive discharges.[7,26,29–32] These modes can exist separately or in combination in a configuration similar to those used in commercial processing tools. Using a multi-frequency self-consistent two-dimensional (2D) hybrid fluid-analytical simulation code in the linearized frequency domain, this type of cylindrical discharge was recently investigated.[33] Since the present version of the code has provisions for up to three input frequencies, we did simulations with a single frequency, and then, using the nonlinear transmission line model[23] to estimate the amplitude and phases of higher harmonics, we explicitly added the most important harmonics as the second and third driving frequencies in a multi-frequency simulation. The results showed that with a single frequency the center-high voltage became important at high frequencies for which the plasma radius was a significant fraction of a wavelength. With the addition of two nonlinearly generated higher harmonics, the center highs were prominent at lower frequencies.

In this work, we analytically treat a model corresponding reasonably closely to both commonly used commercial geometries and to the 2D hybrid simulation code, in order to investigate the frequency effects of the electromagnetic waves and their resonances at high frequencies. In Section II, the configuration is described, the equations to be solved

a)lieber@eecs.berkeley.edu

     23, 013501-1

are derived, and the explanations of the symmetric and anti-symmetric wave modes are given. In Section III, the equations are solved, numerically, for various cases of interest, and the relation of the results to those of the 2D fluid-analytical simulations is explored. Conclusions and further discussion are given in Section IV.

II. MODEL

We consider a cylindrical discharge of radius R and height $2l$, consisting of a sheath-plasma-sheath sandwich between two circular conducting electrodes (see Figure 1). The sheath at the central part (region 1) $0 < r < R_x$ of the lower "powered" electrode is assumed to have a constant width s, independent of r, and the sheath at the outer part (region 2) $R_x < r < R$ of the lower electrode and the entire upper electrode $0 < r < R$ is assumed to have a constant width w. Hence, the plasma extends from $z = -h$ to $z = d$ in region 1 and from $z = -d$ to $z = d$ in region 2, with $h = l - s$ and $d = l - w$. The sheath at the radial wall at $r = R$ must be treated separately, as we do in the analysis. The discharge is driven by a voltage source across a small gap at radial position R_x in the lower electrode. We assume that the excitation voltage is axisymmetric around the circumference, with all system properties independent of the ϕ-coordinate.

A. Basic equations and field solutions

The fields are determined in the lossless limit, and a non-zero loss is only considered for the electron power balance, in Section II B. Here, we assume a uniform lossless bulk plasma having electron density n_e, with relative dielectric constant

$$\kappa_p = 1 - \frac{\omega_p^2}{\omega^2} \tag{1}$$

with $\omega_p = (e^2 n_e / \epsilon_0 m)^{1/2}$ the plasma frequency and ω the applied radio frequency (rf). The sheaths are assumed to

have unity relative dielectric constant. The lengths and frequencies are assumed to be ordered as are typical in most commercial applications

$$w, s \ll l \ll R, \lambda/2\pi, \tag{2}$$

$$\omega_{pi} \ll \omega \ll \omega_{SR}, \tag{3}$$

where $\lambda = 2\pi c/\omega$ is the electromagnetic wavelength, $\omega_{pi} = (e^2 n_e / \epsilon_0 m_i)^{1/2}$ is the ion plasma frequency, and $\omega_{SR} = [(w + s)/2l]^{1/2} \omega_p$ is the series resonance frequency.

The wave propagation is obtained from Maxwell's equations

$$\nabla \times \mathbf{H} = j\omega\epsilon_0\kappa(z)\mathbf{E}, \qquad \nabla \times \mathbf{E} = -j\omega\mu_0\mathbf{H} \tag{4}$$

with $\mathbf{H}$ and $\mathbf{E}$ ($\propto e^{j\omega t}$) the wave magnetic and electric fields, and with $\kappa = \kappa_p$ in the plasma region and $\kappa = 1$ in the sheath regions. We assume a transverse magnetic (TM) mode having only the magnetic field component $H_\phi \sim e^{j\omega t}$. Maxwell equations (4) in both regions 1 and 2 reduce to

$$\frac{\partial H_\phi}{\partial z} = -j\omega\epsilon_0\kappa E_r, \tag{5}$$

$$\frac{1}{r}\frac{\partial(rH_\phi)}{\partial r} = j\omega\epsilon_0\kappa E_z, \tag{6}$$
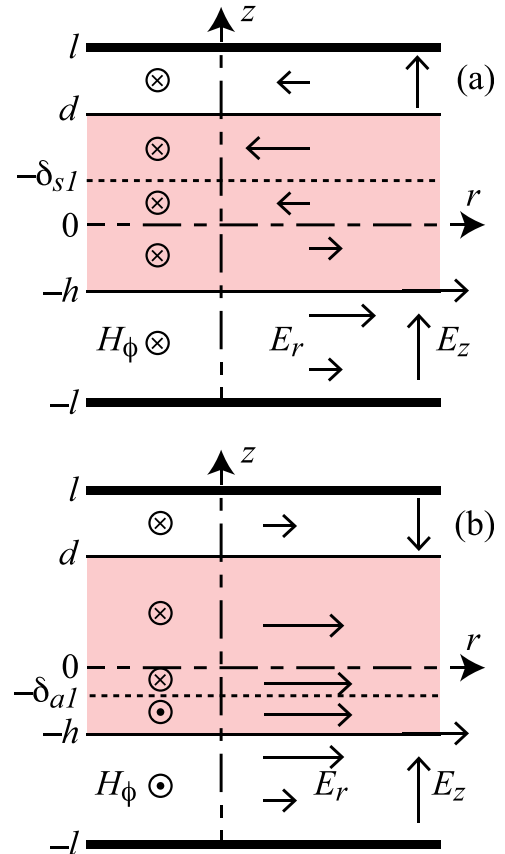
FIG. 2. Illustrating the z-symmetries of the fields for (a) the "quasi-symmetric" and (b) "quasi-antisymmetric" modes in region 1 with unequal sheath widths; in region 2 with equal sheath widths the δ's are zero and the fields are purely symmetric and antisymmetric with respect to $z = 0$; the E_z fields in the plasma are small and not shown.
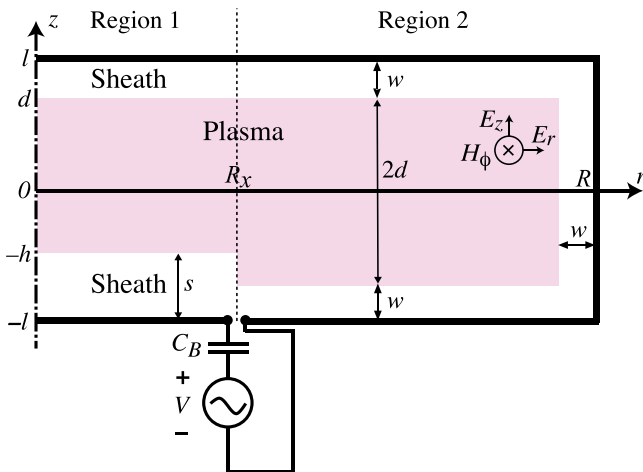

FIG. 1. Asymmetrically driven, cylindrical rf capacitive discharge geometry with two unequal sheath widths, driven by an rf voltage source across an infinitesimal gap at R_x.

$$\frac{\partial E_r}{\partial z} - \frac{\partial E_z}{\partial r} = -j\omega\mu_0 H_\phi. \tag{7}$$

Here, E_z is the capacitive electric field (perpendicular to the discharge plates) and E_r is the inductive field (parallel to the plates). Since E_r and E_z are either in phase or $180°$ out of phase, the electric field is linearly polarized. Substituting for E_r and E_z from (5) and (6) into (7) yields the propagation equation for H_ϕ

$$\frac{\partial}{\partial r}\left[\frac{1}{r\kappa(z)}\frac{\partial(rH_\phi)}{\partial r}\right] + \frac{\partial}{\partial z}\left[\frac{1}{\kappa(z)}\frac{\partial H_\phi}{\partial z}\right] + k_0^2 H_\phi = 0, \tag{8}$$

where $k_0 = \omega/c$ is the free space wavenumber, with c the velocity of light in vacuum.

The two conducting surfaces and the central plasma core form a three-electrode radial transmission line system, and therefore, for $\lambda \gg l$, (8) has two radially propagating mode solutions. All other modes are radially evanescent and are ignored in the development that follows. In region 2, the propagating modes correspond to purely symmetric (s) and purely antisymmetric (a) excitations of the E_z and H_ϕ field components with respect to $z = 0$. In region 1, due to the unequal sheath widths (see Figure 1), the bulk plasma midplane is not symmetric with respect to the discharge electrodes; the modes are "quasi-symmetric" and "quasi-

antisymmetric" with respect to off-set positions $z = -\delta_{s1}$ and $z = -\delta_{a1}$, respectively, which will be determined below. The symmetries of the field components for the symmetric and antisymmetric modes are illustrated in Figure 2.

The fields in the plasma and sheath regions satisfy certain boundary conditions. From (5), the requirement that $E_r = 0$ at the conducting electrodes corresponds to Neumann conditions on H_ϕ

(1) $\partial H_\phi/\partial z = 0$ at $z = \pm l$.
   Additionally, the transverse fields are continuous across the plasma-sheath interfaces
(2) H_ϕ and
(3) E_r are continuous at $z = -h$ and $z = d$ in region 1 and at $z = \pm d$ in region 2.

1. Region 1

For region 1, with $r < R_x$ by symmetry, the H_ϕ field satisfies the condition

(4) $H_\phi = 0$ at $r = 0$.

The solutions of (8) for H_ϕ within the top sheath, the plasma, and the bottom sheath, which satisfy the boundary conditions (1), (2), and (4), are, respectively,

$$H_{\phi 1} = A_{s1}\,\text{sech}\,\beta_{s1}w\cosh\alpha_{s1}(d+\delta_{s1})\cosh\beta_{s1}(l{-}z)\,\text{J}_1(k_{s1}r) \\ + A_{a1}\,\text{sech}\,\beta_{a1}w\sinh\alpha_{a1}(d+\delta_{a1})\cosh\beta_{a1}(l{-}z)\,\text{J}_1(k_{a1}r), \qquad d < z < l, \tag{9}$$

$$H_{\phi 1} = A_{s1}\cosh\alpha_{s1}(z+\delta_{s1})\,\text{J}_1(k_{s1}r) \\ + A_{a1}\sinh\alpha_{a1}(z+\delta_{a1})\,\text{J}_1(k_{a1}r), \qquad -h < z < d, \tag{10}$$

$$H_{\phi 1} = A_{s1}\,\text{sech}\,\beta_{s1}s\cosh\alpha_{s1}(h{-}\delta_{s1})\cosh\beta_{s1}(l+z)\,\text{J}_1(k_{s1}r) \\ - A_{a1}\,\text{sech}\,\beta_{a1}s\sinh\alpha_{a1}(h{-}\delta_{a1})\cosh\beta_{a1}(l+z)\,\text{J}_1(k_{a1}r), \qquad -l < z < -h, \tag{11}$$

where A_{s1} and A_{a1} are the symmetric and antisymmetric mode coefficients, J_1 is the first order Bessel function of the first kind, k_{s1} and k_{a1} are the radial wavenumbers, α_{s1} and α_{a1} are the axial decay constants in the plasma region, and β_{s1} and β_{a1} are the axial decay constants in the sheath regions. The corresponding E_r and E_z fields are found by substituting expressions (9)–(11) into (5) and (6), respectively, and are given in Appendix A.

From (8), the symmetric and antisymmetric axial decay constants (α_s and α_a in the plasma and β_s and β_a in the sheaths) are related to their respective radial wavenumbers in the plasma and in the sheaths by

$$k^2 = \alpha^2 + k_0^2\kappa_p, \tag{12}$$
$$k^2 = \beta^2 + k_0^2. \tag{13}$$

Evaluating the final boundary condition (3) that E_r be continuous at $z = d$ and $z = -h$ for the symmetric mode using expressions (A1)–(A3), we obtain

$$\kappa_p\beta_{s1}\tanh\beta_{s1}w + \alpha_{s1}\tanh\alpha_{s1}(d+\delta_{s1}) = 0, \tag{14}$$

$$\kappa_p\beta_{s1}\tanh\beta_{s1}s + \alpha_{s1}\tanh\alpha_{s1}(h-\delta_{s1}) = 0. \tag{15}$$

Similarly, for the antisymmetric mode, we obtain

$$\kappa_p\beta_{a1}\tanh\beta_{a1}w + \alpha_{a1}\coth\alpha_{a1}(d+\delta_{a1}) = 0, \tag{16}$$

$$\kappa_p\beta_{a1}\tanh\beta_{a1}s + \alpha_{a1}\coth\alpha_{a1}(h-\delta_{a1}) = 0. \tag{17}$$

Solving (12)–(15) yields k_{s1}, α_{s1}, β_{s1}, and δ_{s1} for the symmetric mode. Similarly, solving (12), (13), (16), and (17) yields k_{a1}, α_{a1}, β_{a1}, and δ_{a1} for the antisymmetric mode. These equations are solved numerically in Section III. For a low density plasma, assuming that the skin depth α^{-1} is large compared to l, we can take $\tanh(x) \to x$ and $\coth(x) \to 1/x$ in (14)–(17), to obtain approximate solutions, which are given in Appendix B.

2. Region 2

For the outer region 2 with $r > R_x$, the top and bottom sheath widths are equal and the H_ϕ and E_z fields of the two propagating modes are either purely symmetric or antisymmetric with respect to $z = 0$, as illustrated in Figure 2. H_ϕ in

region 2 is the same as in region 1 except that in (9)–(11), $s \to w$ and $h \to d$, the δ's are zero, and the radial variation changes from the J_1 Bessel function to a linear combination of Bessel functions of the first and second kinds

$$J_1 \to J_1 + bN_1 \qquad (18)$$

with b a coefficient determined below. The H_ϕ fields in region 2 are

$$H_{\phi 2} = A_{s2} \operatorname{sech} \beta_{s2} w \cosh \alpha_{s2} d \cosh \beta_{s2}(l\text{–}z)\,(J_1(k_{s2}r)+b_{s2}N_1(k_{s2}r)) \\ + A_{a2} \operatorname{sech} \beta_{a2} w \sinh \alpha_{a2} d \cosh \beta_{a2}(l\text{–}z)\,(J_1(k_{a2}r)+b_{a2}N_1(k_{a2}r)), \qquad d < z < l, \qquad (19)$$

$$H_{\phi 2} = A_{s2} \cosh \alpha_{s2} z\,(J_1(k_{s2}r)+b_{s2}N_1(k_{s2}r)) \\ + A_{a2} \sinh \alpha_{a2} z\,(J_1(k_{a2}r)+b_{a2}N_1(k_{a2}r)), \qquad -d < z < d, \qquad (20)$$

$$H_{\phi 2} = A_{s2} \operatorname{sech} \beta_{s2} w \cosh \alpha_{s2} d \cosh \beta_{s2}(l+z)\,(J_1(k_{s2}r)+b_{s2}N_1(k_{s2}r)) \\ - A_{a2} \operatorname{sech} \beta_{a2} w \sinh \alpha_{a2} d \cosh \beta_{a2}(l+z)\,(J_1(k_{a2}r)+b_{a2}N_1(k_{a2}r)), \qquad -l < z < -d. \qquad (21)$$

The corresponding E_r and E_z fields in region 2 are found by substituting expressions (19)–(21) into (5) and (6), respectively, and are given in Appendix A.

The coefficient b is determined by the radial transmission line boundary condition at $r = R$, which is different for the two modes. For the E_z-symmetric mode, the voltages across the upper and lower halves of the discharge are equal, $V_z = -\int_0^l dz\, E_{z2} = -\int_{-l}^0 dz\, E_{z2}$, as seen in Figure 2. Since the total voltage across the electrodes must vanish at the conducting radial wall, we use a short circuit boundary condition

(5) $E_{z2} = 0$ at $r = R$ for the symmetric mode.

Boundary condition 5 applied to the sheath E_z field (A10) or (A12) yields the symmetric mode coefficient

$$b_{s2} = -\frac{J_0(k_{s2}R)}{N_0(k_{s2}R)}. \qquad (22)$$

For the antisymmetric mode, the r-directed surface current densities flowing in the upper and lower electrodes are equal, $K_r = H_{\phi 2}(R, l) = -H_{\phi 2}(R, -l)$. By symmetry, the current must vanish at the radial wall at $z = 0$. We use an open circuit boundary condition, assuming that the sheath reactance magnitude $|X_{\text{wall}}|$ at the radial wall is much larger than the characteristic impedance Z_0 of the radial transmission line at $r = R$

(5′) $H_{\phi 2} = 0$ at $r = R$ for the antisymmetric mode.

Estimating

$$|X_{\text{wall}}| = \frac{1}{\omega C_{\text{wall}}} \approx \frac{w}{\omega \epsilon_0 \cdot 2\pi R \cdot 2l}, \qquad (23)$$

and from transmission line theory

$$Z_0 \approx \frac{1}{2\pi R}\left(\frac{\mu_0}{\epsilon_0}\frac{lw}{2}\right)^{1/2}, \qquad (24)$$

we obtain the ratio

$$\frac{|X_{\text{wall}}|}{Z_0} \approx \frac{\lambda}{2\pi l}\left(\frac{2w}{l}\right)^{1/2}. \qquad (25)$$

Since $\lambda/2\pi l \gg 1$ from (2), we see that $|X_{\text{wall}}| \gg Z_0$, as required. Boundary condition (5′) applied to (19) or (21) yields the antisymmetric mode coefficient

$$b_{a2} = -\frac{J_1(k_{a2}R)}{N_1(k_{a2}R)}. \qquad (26)$$

As in region 1, the symmetric and antisymmetric axial decay constants in region 2 are related to their respective plasma and sheath radial wavenumbers by (12) and (13). Evaluating the final boundary condition (3) that E_r be continuous at $z = \pm d$, and using expressions (A7)–(A9), we obtain

$$\kappa_p \beta_{s2} \tanh \beta_{s2} w + \alpha_{s2} \tanh \alpha_{s2} d = 0 \qquad (27)$$

for the symmetric mode, and

$$\kappa_p \beta_{a2} \tanh \beta_{a2} w + \alpha_{a2} \coth \alpha_{a2} d = 0 \qquad (28)$$

for the antisymmetric mode. Solving (12), (13), and (27) yields k_{s2}, α_{s2}, and β_{s2} for the symmetric mode. Similarly, solving (12), (13), and (28) yields k_{a2}, α_{a2}, and β_{a2} for the antisymmetric mode. The equations are solved numerically in Section III. For a low density plasma with a skin depth large compared to l, we can take $\tanh(x) \to x$ and $\coth(x) \to 1/x$ in (27) and (28), to obtain approximate solutions, which are given in Appendix B.

There are four undetermined mode coefficients, A_{s1}, A_{s2}, A_{a1}, A_{a2}, so four conditions are required to "join" the solution in region 1 to that in region 2:

(a) The current density in the top electrode is continuous

$$H_{\phi 1}(R_x, l) = H_{\phi 2}(R_x, l). \qquad (29)$$

(b) The current density in the bottom electrode is continuous

$$H_{\phi 1}(R_x, -l) = H_{\phi 2}(R_x, -l). \qquad (30)$$

(c)   The top plasma-to-sheath voltage is continuous

$$\int_d^l dz\, [E_{z1}(R_x, z) - E_{z2}(R_x, z)] = 0. \qquad (31)$$

(d)   The bottom plasma-to-sheath voltage difference is equal to the applied source voltage V

$$\int_{-l}^{-d} dz\, [E_{z2}(R_x, z)] - \int_{-l}^{-h} dz\, E_{z1}(R_x, z)] = V. \qquad (32)$$

Note that because $\omega \ll \omega_{\mathrm{SR}}$, the small voltage drop across the plasma has been neglected. The inhomogeneous system of equations (29)–(32) is linear in the mode coefficients and has the form

$$\mathbf{M} \cdot \mathbf{A} = \mathbf{V}, \qquad (33)$$

where $\mathbf{M}$ is the 4×4 coefficient matrix, $\mathbf{A}$ is the 4×1 column vector of mode coefficients, and $\mathbf{V}$ is the 4×1 column vector of the voltage excitation. (The first three elements of $\mathbf{V}$ are zero and the last element is V.) The solutions for the mode coefficients are obtained numerically in Section III.

B. Child law and electron power balance

For any specified powered and grounded sheath widths s and w and applied rf voltage V, the mode coefficients are found by solving the four linear equations (29)–(32). However, these solutions are not generally consistent with the specified values of s, w, and V. We use the Child laws at the two sheaths and the global (volume-averaged) electron power balance to determine self-consistent values for s, w, and V.

The ion current density lost to each electrode is $J_i = e h_l n_e u_B$, where $h_l = 0.86/(3 + l/\lambda_i)^{1/2}$ is the edge-to-center density ratio, with λ_i the ion-neutral mean free path, and $u_B = (e\mathrm{T}_e/m_i)^{1/2}$ is the Bohm (ion loss) velocity, with T_e the electron temperature. The collisionless Child law for an rf sheath then specifies s and w in terms of the average voltage across the powered and grounded electrodes

$$s = \frac{K_{\mathrm{CL}}}{1.23} \left(\frac{\int_0^{R_x} dr\, |V_b(r)|}{R_x} \right)^{3/4} + 2.61\,\lambda_D, \qquad (34)$$

$$w = \frac{K_{\mathrm{CL}}}{1.23} \left(\frac{\int_{R_x}^R dr\, |V_b(r)| + \int_0^R dr\, |V_t(r)|}{2R - R_x} \right)^{3/4} + 2.61\,\lambda_D, \qquad (35)$$

where

$$K_{\mathrm{CL}} = 0.79 \left(\frac{\epsilon_0}{J_i} \right)^{1/2} \left(\frac{2e}{m_i} \right)^{1/4}, \qquad (36)$$

V_t and V_b are the radially varying voltages across the top $(z = l)$ and bottom $(z = -l)$ sheaths with respect to their respective electrode surfaces, and $\lambda_D = (\epsilon_0 \mathrm{T}_e/e h_l n_e)^{1/2}$ is the electron Debye length at the plasma-sheath edge. The factor of 1.23 in (34) and (35) converts the maximum to the time-average sheath width, and the last term ($2.61\,\lambda_D$) specifies a minimum sheath width when the rf sheath voltage is zero.[15,16]

Since $V \to 0$ at resonance, we do not choose V, but rather specify an electron density n_e, or equivalently, the electron power lost

$$P_{e,\mathrm{lost}} = J_i \mathcal{E}_e \cdot 2\pi R^2, \qquad (37)$$

where $\mathcal{E}_e = \mathcal{E}_c + 7.2\,\mathrm{T}_e$ is the total electron energy lost per electron-ion pair created, $\mathcal{E}_c$ is the collisional electron energy lost per electron-ion pair created, and $7.2\,\mathrm{T}_e$ gives the electron energy carried across the sheath to the electrode surface. (The total power lost also includes ion power losses to the electrode, which we do not consider here.) For argon, we have $\mathcal{E}_c = 15.79 + 12.14 K_{\mathrm{exc}}/K_{\mathrm{iz}} + 4.08 \times 10^{-5} \mathrm{T}_e K_{\mathrm{elas}}/K_{\mathrm{iz}}$, where $K_{\mathrm{iz}} = 2.34 \times 10^{-14} \mathrm{T}_e^{0.59} e^{-17.44/\mathrm{T}_e}$ m³/s, $K_{\mathrm{exc}} = 2.48 \times 10^{-14} \mathrm{T}_e^{0.33} e^{-12.78/\mathrm{T}_e}$ m³/s, and $K_{\mathrm{elas}} = 1.619 \times 10^{-14} \mathrm{T}_e^{1.566} e^{0.0207(\ln \mathrm{T}_e)^2 - 0.1047(\ln \mathrm{T}_e)^3}$ m³/s are fits to the ionization, excitation, and elastic scattering rate coefficients for argon over the T_e range from 1 to 7V (see Ref. 1, Sec. 3.5. We do not solve a global particle balance for the discharge, but use a nominal temperature $\mathrm{T}_e = 3.5$ V in the calculations, consistent with the fluid simulations at 10 mTorr (see below).

The electron power absorbed is the sum of ohmic and stochastic heating powers calculated from the fields for a given s, w, and V

$$P_{e,\mathrm{abs}} = P_{\mathrm{ohm},z} + P_{\mathrm{ohm},r} + P_{\mathrm{stoc}}. \qquad (38)$$

The ohmic powers are

$$P_{\mathrm{ohm},z} = \int\limits_{\substack{\mathrm{plasma} \\ \mathrm{volume}}} d\mathcal{V} \frac{|J_z|^2}{2\sigma_{\mathrm{dc}}}, \qquad (39)$$

$$P_{\mathrm{ohm},r} = \int\limits_{\substack{\mathrm{plasma} \\ \mathrm{volume}}} d\mathcal{V} \frac{|J_r|^2}{2\sigma_{\mathrm{dc}}}, \qquad (40)$$

where $\sigma_{\mathrm{dc}} = e^2 n_e/m\nu_{\mathrm{elas}}$ is the dc plasma conductivity, with $\nu_{\mathrm{elas}} = K_{\mathrm{elas}} n_g$ the electron-neutral collision frequency at the gas density n_g. The stochastic heating is expressed in terms of the bottom and top sheath voltages

$$P_{\mathrm{stoc}} = K_{\mathrm{stoc}} \int_0^R dr\, 2\pi r(|V_b(r)| + |V_t(r)|), \qquad (41)$$

where $K_{\mathrm{stoc}} = 0.45\,\epsilon_0 \omega^2 (m\mathrm{T}_e/e)^{1/2}$ (see Ref. 1, Sec. 11.2). Equating (37) to (38) gives the electron power balance. Summarizing, for a given n_e, the Child law relations (34) and (35), along with the electron power balance, are used to determine self-consistent values of s, w, and V.

III. NUMERICAL SOLUTIONS

The procedure for self-consistently solving the electromagnetics, the nonlinear Child laws, and electron power

balance is described in Appendix C. We choose a geometry with half-length $l = 2.5$ cm, discharge radius $R = 25$ cm, and powered electrode radius $R_x = 15$ cm. We also compare the results for the sheath widths, source voltage, and sheath voltage ratios to self-consistent 2D hybrid fluid-analytical electromagnetic simulations[15,16] (symbols in the figures). The same geometry is used, except that the voltage excitation is over a gap from $r = 15$ to 17 cm. We note that the field solve in the simulations includes the power losses and the radially evanescent modes; both are absent in the analytical model. In addition, the self-consistent sheath widths in the simulations vary with r and also exist along the outside conductor at $r = R$, and the electron density and temperature also vary within the plasma. In order to make the comparisons with the model results, the simulation sheath widths are radially averaged. Figures 3–7 give the discharge characteristics (lines) at 10 mTorr for a density $n_e = 1 \times 10^{16}$ m^{-3} ($P_e = 68$ W) over the 30–120 MHz frequency range. As shown in Figure 3(a), at low frequencies, the powered electrode sheath width s is significantly larger than the grounded electrode sheath width w. The two sheath widths become and remain comparable above about 50 MHz. The fluid simulation results (symbols), obtained at a central ($r = 0$, $z = 0$) density of 1×10^{16} m^{-3}, generally track the model sheath widths, but there are some differences, due partially to the nonuniform spatial density

and temperature profiles determined in the simulations. For example, the increase in s from 70 to 72.5 MHz in the simulation results is associated with a transition from a center-low to center-high simulation density profile, along with an electron power decrease from 85 to 47 W; these density profile-dependent variations are, of course, absent in the constant density and power analytical model results. The rf source voltage V in Figure 3(b) (solid line) is seen to decrease with the increasing frequency in the low frequency range and displays three resonances at 61.5, 88.5, and 103.55 MHz. We compare this voltage variation to the reactive (dots) and total (squares) source voltages determined from the fluid simulations. These are defined as $V_{\text{reac}} = X \cdot |I|$ and $V_{\text{tot}} = |(R + jX) \cdot I|$, where R and X are the discharge input resistance and reactance (ohms) seen at the source terminals and I is the (complex) source current. The reactive voltage is seen to track the model results quite well and exhibits the minima associated with the first anti-symmetric and symmetric resonances; in contrast, these minima are barely seen in the total voltage, due to the finite discharge resistance.

The radial wavenumbers in regions 1 and 2 shown in Figures 3(c) and 3(d) give an understanding of the source of the resonances. (The wavenumbers in regions 1 and 2 differ somewhat because of the differing sheath widths; this difference is ignored in the estimate that follows.) The first
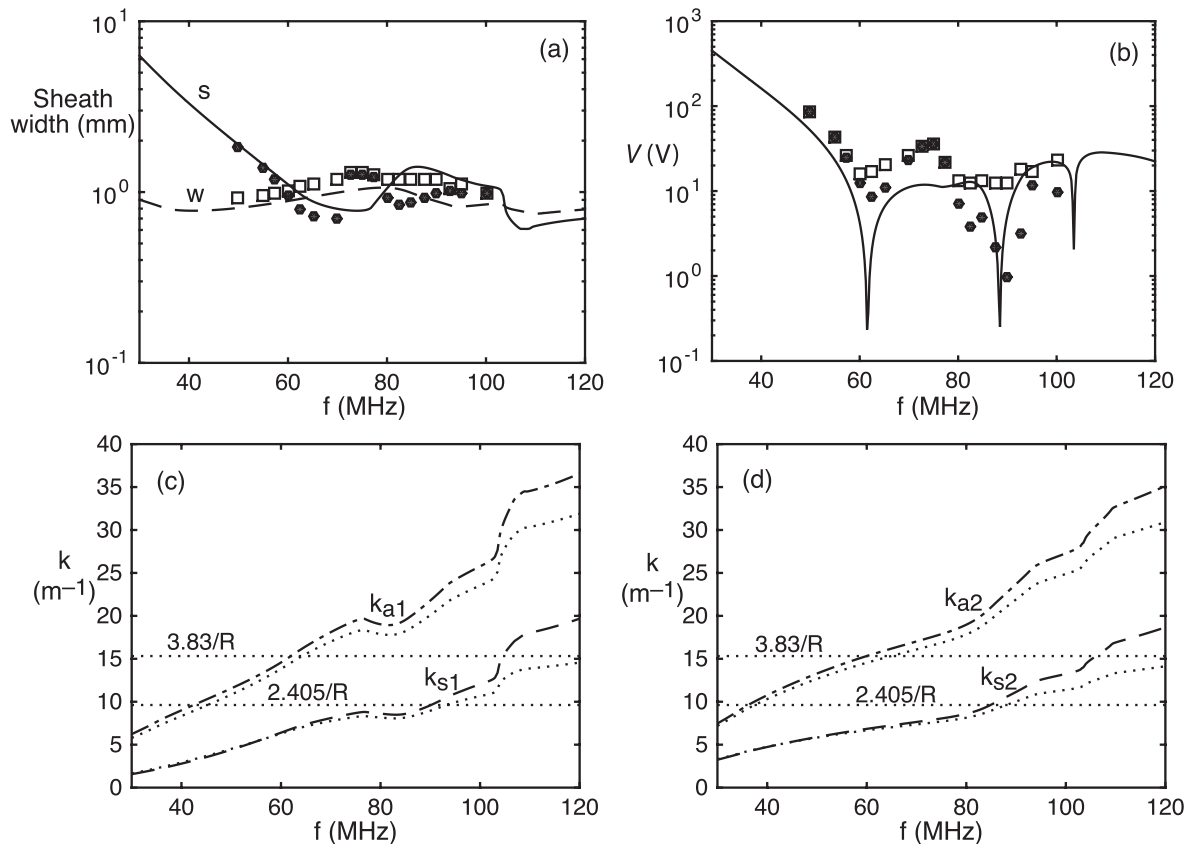

FIG. 3. Density $n_e = 1 \times 10^{16}$ m^{-3} (68 W electron power), showing the frequency variation of (a) the sheath widths s and w (lines and symbols give model and fluid simulation results); (b) the excitation voltage V; the line gives the model results, the symbols give the reactive (dots) and total (open squares) excitation voltage from the simulations; (c) and (d) the model symmetric (dashed) and antisymmetric (dotted-dashed) radial wavenumbers k_s and k_a in regions 1 and 2; the dotted lines following these curves give the approximate solutions of Appendix B.
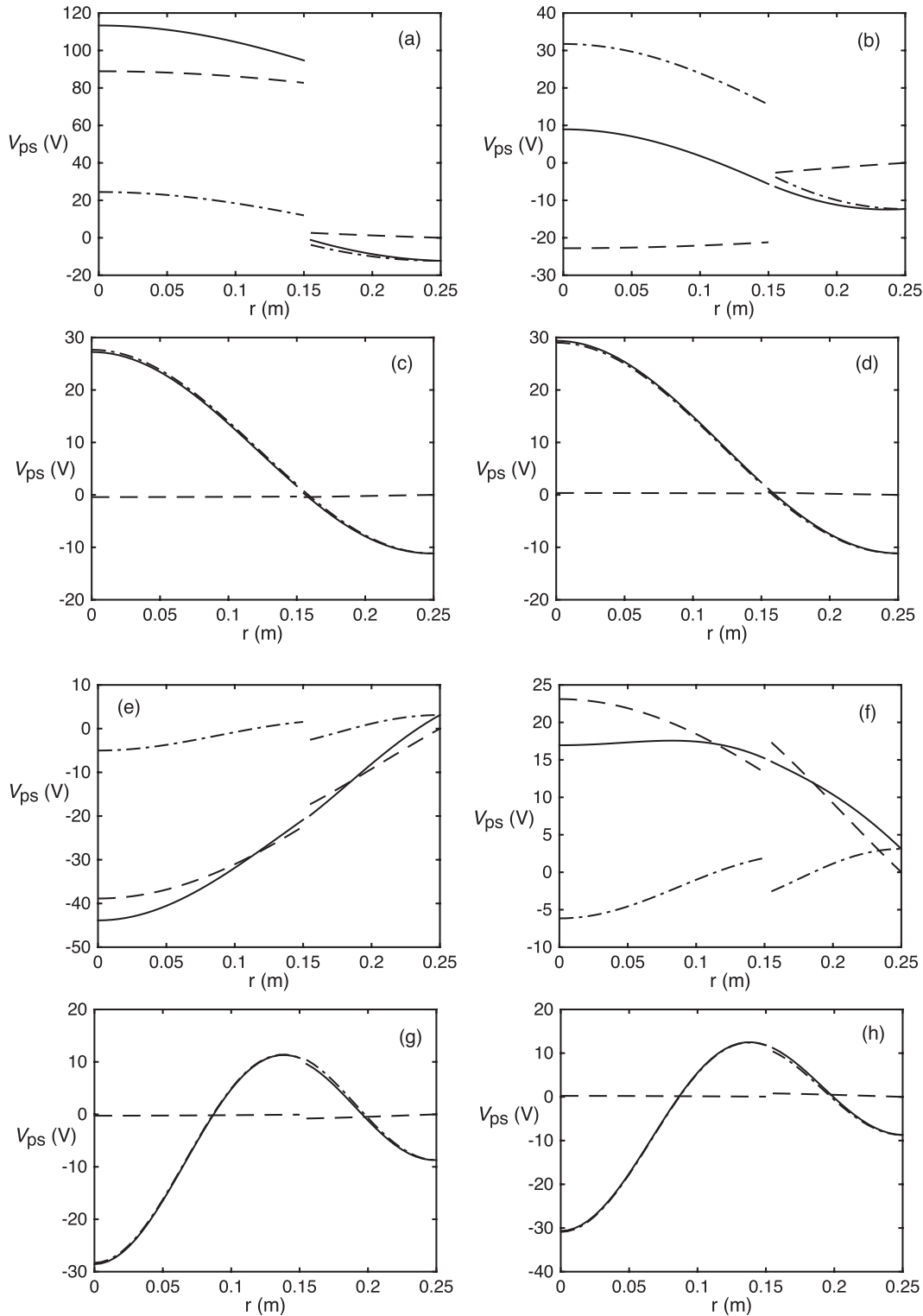
FIG. 4. Plasma-to-sheath voltages V_{ps} for $n_e = 1 \times 10^{16}$ m^{-3}: (a) and (b) at the bottom and top electrodes at 45 MHz; (c) and (d) at the bottom and top electrodes for the first antisymmetric resonance at 61.5 MHz; the dashed and dotted-dashed lines show the symmetric and antisymmetric modes and the solid line shows the total. Plasma-to-sheath voltages V_{ps} for $n_e = 1 \times 10^{16}$ m^{-3}: (e) and (f) at the bottom and top electrodes for the first symmetric resonance at 88.5 MHz; (g) and (h) at the bottom and top electrodes for the second antisymmetric resonance at 103.55 MHz; the dashed and dotted-dashed lines show the symmetric and antisymmetric modes and the solid line shows the total.

antisymmetric mode resonance is at $k_a \approx \chi_{11}/R$, where $\chi_{11} \approx 3.83$ is the first zero of $J_1(\chi) = 0$. We see in Figures 3(c) and 3(d) that this occurs at about 61.5 MHz, which is the lowest resonance in Figure 3(b). The first symmetric mode resonance is at $k_s \approx \chi_{01}/R$, where $\chi_{01} = 2.405$

is the first zero of $J_0(\chi) = 0$. We see this crossing in Figures 3(c) and 3(d) at about 88.5 MHz, which is the next higher frequency resonance shown in Figure 3(b). Higher order resonances can be found similarly; the second antisymmetric resonance at $k_a \approx \chi_{12}/R$, with $\chi_{12} \approx 7.02$, is shown in
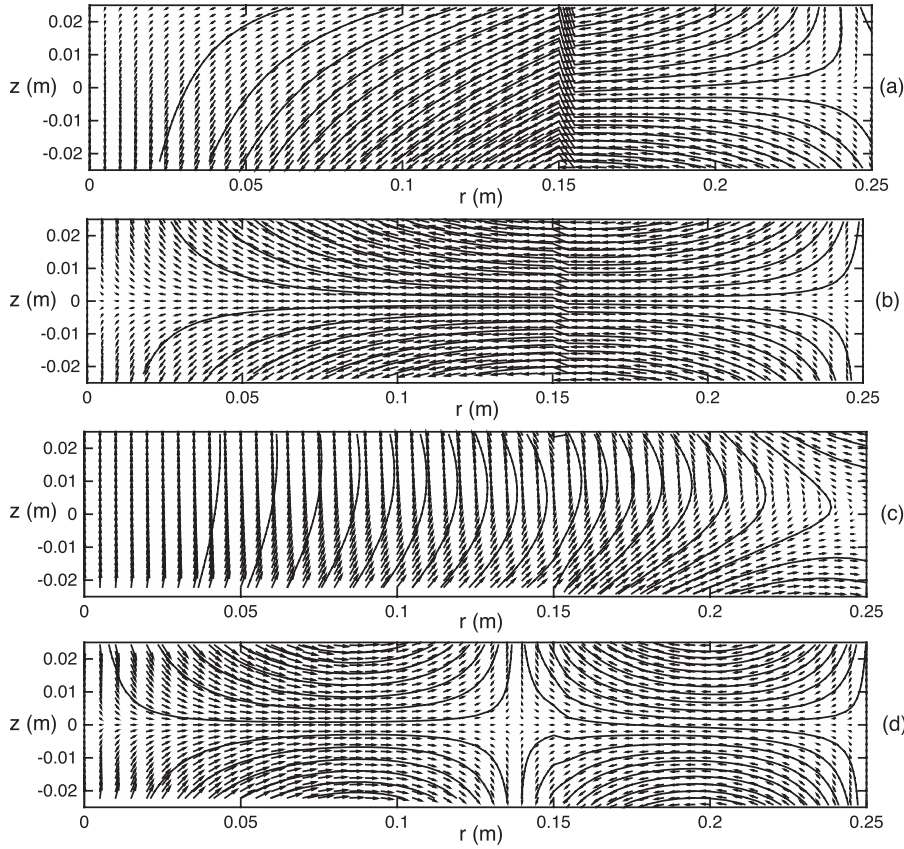
FIG. 5. Density $n_e = 1 \times 10^{16}$ m^{-3} (68 W electron power), showing the E-field lines in the plasma (solid) and the amplitude and direction of the E-fields (arrows) for (a) 45 MHz, (b) the first antisymmetric resonance at 61.5 MHz, (c) the first symmetric resonance at 88.5 MHz, and (d) the second antisymmetric resonance at 103.55 MHz.

Figure 3(b). The ordering of the resonances with frequency can be understood from approximate expressions for the radial wavenumbers given in Appendix B. Equating k_{a1}^2 in (B6) to χ_{11}^2/R^2, neglecting the small k_0^2 term, setting $h \approx d \approx l$, and using $\kappa_p \approx -\omega_p^2/\omega^2$, we obtain

$$k_{a1}^2 = \frac{\omega_a^2}{\omega_p^2} \frac{s+w}{2swl} = \frac{\chi_{11}^2}{R^2}, \qquad (42)$$

where ω_a is the first antisymmetric resonance frequency. Similarly equating k_{s1}^2 in (B2) to χ_{01}^2/R^2, with $k_0^2 = \omega_s^2/c^2$, we obtain

$$k_{s1}^2 = \frac{\omega_s^2}{c^2} \frac{2l}{s+w} = \frac{\chi_{01}^2}{R^2}, \qquad (43)$$

where ω_s is the first symmetric resonance frequency. Solving (42) and (43) for the frequency ratio, we obtain

$$\frac{\omega_a}{\omega_s} = \frac{\chi_{11}}{\chi_{01}} \frac{l}{\delta_p} \frac{2\sqrt{sw}}{s+w}, \qquad (44)$$

where $\delta_p = c/\omega_p$ is the collisionless skin depth. At $n_e = 1 \times 10^{16}$ m^{-3}, $\delta_p \approx 5.3$ cm. Substituting this into (44) and taking for a simple estimate the nominal values $s \approx w \approx 1$ mm, we find that $\omega_a/\omega_s \approx 0.75$, i.e., the first resonance encountered as the frequency is increased is antisymmetric. The actual ratio seen in Figure 3(b) is 0.69, in reasonable agreement with the estimate. The condition for a double resonance, $\omega_a = \omega_s$, is found from (44) to be $\delta_p \approx 4.0$, which corresponds to $n_e \approx 1.8 \times 10^{16}$ m^{-3}. This condition underestimates the numerically calculated density of 3.3×10^{16} m^{-3}

from the analytic model, mainly due to the assumption that $\delta_p \gg l$ in the approximate k's used to obtain (42) and (43), whereas $\delta_p \sim l$ at the double resonance.

The radial variations of the plasma-sheath voltages V_{ps} at the bottom and top electrodes are given in Figure 4 at a low frequency of 45 MHz, and at the three resonance frequencies of 61.5, 88.5, and 103.55 MHz. In Figure 4(a), the symmetric voltage dominates on the powered electrode, although the smaller antisymmetric voltage, with a shorter wavelength, contributes significantly to the radial variation of the total voltage. The source voltage is 94.8 V, and there is a strong powered-to-grounded voltage asymmetry. As shown in Figures 4(a) and 4(b), the symmetric and antisymmetric voltages nearly cancel on the grounded electrode. In Figures 4(c) and 4(d), at the first antisymmetric resonance of 61.5 MHz, the source voltage is negligible, and the symmetric mode amplitude is nearly zero; the bottom and top sheath voltages are nearly identical and display a $J_0(k_a r)$ Bessel function variation with $k_a R = \chi_{11} \approx 3.83$ (the first zero of J_1). In Figures 4(e) and 4(f), at the first symmetric resonance of 88.5 MHz, the source voltage is negligible and the antisymmetric mode amplitude is small, but not negligible, because an antisymmetric mode component is required to carry current from the central region 1 into the edge region 2. The bottom and top sheath voltages are 180° out-of-phase, indicating that the symmetric mode dominates. There is an approximate $J_0(k_s r)$ Bessel function variation with $k_s R = \chi_{01} \approx 2.405$ (the first zero of J_0), but the antisymmetric component distorts this shape considerably at the top electrode. In Figures 4(g) and 4(h), at the second antisymmetric resonance of 103.55 MHz, the source voltage is negligible and
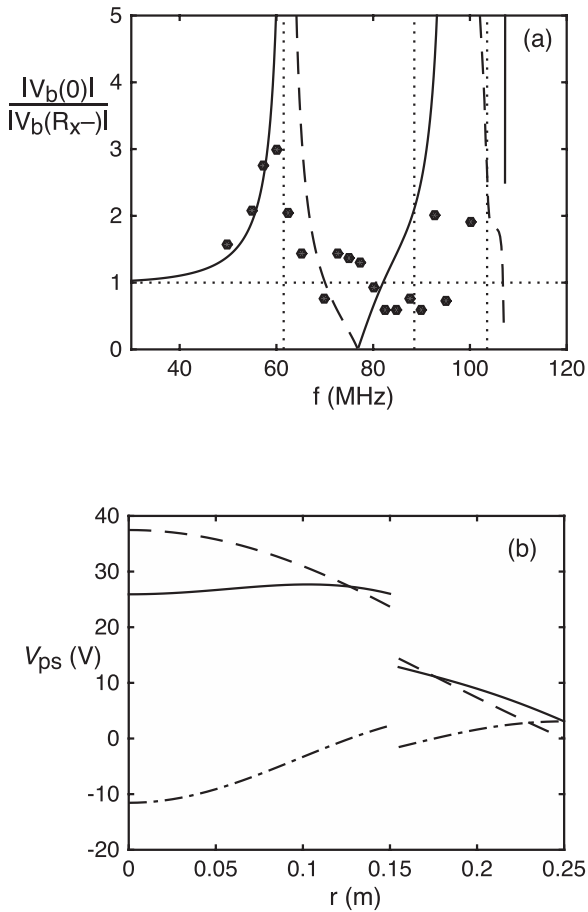
FIG. 6. Density $n_e = 1 \times 10^{16}$ m^{-3}, showing (a) the frequency variation of the magnitude of the center-to-edge voltage ratio $V_b(0)/V_b(R_x-)$ at the powered ($r < R_x$) electrode (solid and dashed lines indicate positive and negative values); the vertical dotted lines give the first antisymmetric resonance at 61.5 MHz, the first symmetric resonance at 88.5 MHz, and the second antisymmetric resonance at 103.55 MHz; (b) the plasma-to-sheath voltage at the bottom (powered) electrode at 82 MHz where $V_b(0)/V_b(R_x-) = 1$; the dashed and dotted-dashed lines show the symmetric and antisymmetric modes and the solid line gives the total.

the symmetric mode amplitude is nearly zero; the bottom and top sheath voltages are nearly identical, as they are at the first antisymmetric resonance, and display a $J_0(k_a r)$ Bessel function variation with $k_a R \approx \chi_{12} \approx 7.02$ (the second zero of J_1).

Figure 5 shows the E-field lines in the plasma (solid) and the magnitude and direction of the E-fields (small arrows) at 45, 61.5, 88.5, and 103.55 MHz. The field lines are found from the constant rH_ϕ condition

$$d(rH_\phi) = \frac{\partial(rH_\phi)}{\partial r} dr + \frac{\partial(rH_\phi)}{\partial z} dz = 0. \qquad (45)$$

Substituting (5) and (6) into (45), we obtain the field line equation

$$\frac{dr}{dz} = \frac{E_r}{E_z}. \qquad (46)$$

Figure 5(a) gives the 45 MHz case, which is mainly symmetric and is quite characteristic of the usual low frequency capacitive discharge regime; we see that the E_z-fields at the
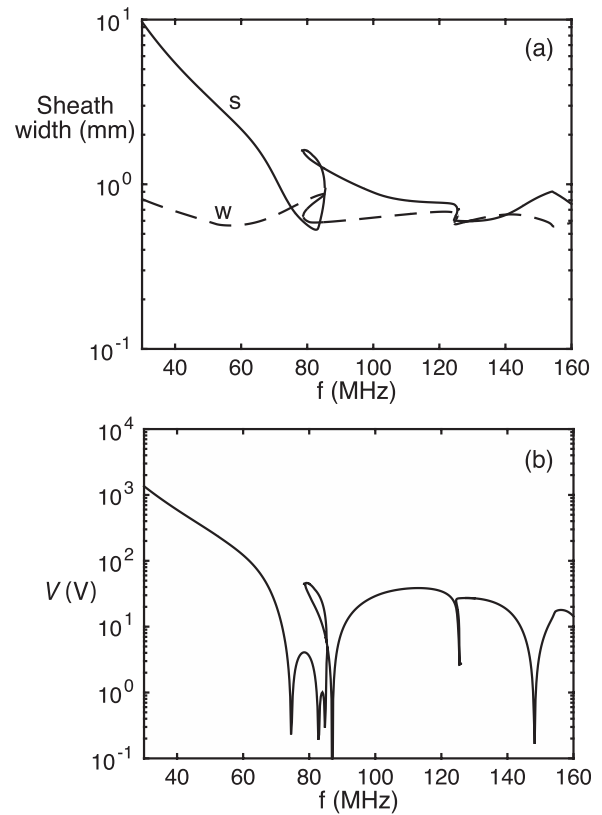

FIG. 7. Density $n_e = 2 \times 10^{16}$ m^{-3} (170 W electron power), showing the frequency variation of (a) the sheath widths s and w, and (b) the excitation voltage V; a discharge hysteresis is observed between 75 and 86.5 MHz.

bottom and top electrodes in region 1 are in-phase; however, there is a significant antisymmetric mode component, which supports the flow of rf plasma current from region 1 into the peripheral region 2, where the fields are mainly antisymmetric. (The field discontinuity at $r = R_x$ is due to the sudden sheath width change from s to w at the lower electrode and the neglect of the radially evanescent modes in the electromagnetics model.) Figure 5(b) at 61.5 MHz shows the expected strongly antisymmetric field structure at the first antisymmetric resonance. Figure 5(c) at 88.5 MHz shows the mainly symmetric field structure expected at the first symmetric resonance; some antisymmetric character is seen near the radial edge $r = R$. Figure 5(d) at 103.55 MHz shows the expected strongly antisymmetric field structure at the second antisymmetric resonance; we see the two radial periods of the antisymmetric mode.

The center-to-edge voltage ratio $V_b(0)/V_b(R_x-)$ at the powered electrode, $r < R_x$, and more generally, the sheath voltage radial variation, is of interest in various processing applications that require high uniformity. Figure 6(a) shows the voltage ratio as the frequency is varied from 30 to 120 MHz, with solid and dashed lines labeling positive and negative ratios. The vertical dotted lines give the locations of the resonances shown in Figure 3(b). We see that the voltage ratio rises from unity at low frequencies and tends to infinity just beyond the first (61.5 MHz) antisymmetric resonance. This represents an "apparent" resonance of the powered electrode alone, with $J_0(k_a R_x) \to 0$, giving a strong nonuniformity at the powered electrode, but it is not an actual resonance

of the discharge. The near-coincidence of this apparent powered electrode resonance to the actual antisymmetric resonance at 61.5 MHz is fortuitous; it is due to the choices of $R = 25$ cm and $R_x = 15$ cm. For these values, the antisymmetric resonance has a zero at $r/R = \chi_{01}/\chi_{11} \approx 0.63$, while the apparent local resonance has a zero at $r/R = R_x/R = 0.6$. We did calculations with R_x varying from 7 cm to 22 cm to confirm this feature of the solution. We found, as expected, that at an actual resonance, the source voltage vanishes, such that the fields (and the resonant frequency) do not depend on R_x; however, the fields and frequency of the apparent local resonance of the powered electrode do depends on the choice of R_x. The apparent resonance frequency was within 10% of the actual resonance frequency over the range of 7 to 22 cm.

We also compare the model results in Figure 6(a) to the fluid simulation results for the magnitude of the ratio of the total sheath voltages, $|V_b(0)/V_b(15\,\mathrm{cm})|$ (dots). We see a good correspondence between the model and simulation near the first antisymmetric resonance, but some differences are seen at frequencies above 70 MHz. The simulations do not show the minimum near 77 MHz and only hint at the apparent resonance at 97.5 MHz seen in the model. We ascribe these differences to rapid radial variations of the sheath voltage near the dielectric spacer in the simulations. Near a resonance, the sheath voltages at both terminals of the source are nearly the same, but away from resonance, the sheath voltage varies rapidly across the source terminals, giving a large uncertainty in the voltage ratio. These phenomena can be seen in Figure 6(b) at 82 MHz, where the voltage ratio is predicted to be unity in the model. We see a quite flat sheath voltage profile on the powered electrode (solid line), with the radial variations of the symmetric and antisymmetric modes nearly cancelling. There is a large sheath voltage across the source gap in this nonresonant case. A large voltage is found across the quartz spacer "gap" from 15 to 17 cm in the fluid simulations.

Additional features of the electromagnetics solutions at a higher density of $n_e = 2 \times 10^{16}$ m^{-3} ($P_e = 170$ W) are shown in Figure 7, over the range of 30–160 MHz. The most notable new feature is the existence of multiple equilibria between approximately 75 and 86.5 MHz, leading to the appearance of additional resonances. The first resonance is the antisymmetric mode; its frequency has increased from 61.5 MHz to 74.5 MHz with the factor-of-two density increase, in rough agreement with the scaling given in (42). The frequency of the first symmetric mode has barely changed, from 88.5 to 87 MHz, nearly independent of the factor-of-two density increase, in agreement with (43). The two resonances at 82.75 and 84.75 MHz, lying between the first antisymmetric and first symmetric modes, are hybrid combinations of these modes, exhibiting hysteresis. Also seen are the second antisymmetric resonance at 125.45 MHz and the second symmetric resonance at 148.25 MHz. Figure 8 shows a comparison of the model and fluid simulation results over a somewhat smaller range of 40 to 100 MHz, to emphasize the important details. We find a reasonable correspondence for the sheath widths and for the reactive voltage variations in the simulations. The total voltage variations only hint at these voltage minima, due to the resistive voltage component. We searched for, but did not find, evidence of multiple equilibria in the fluid simulations.
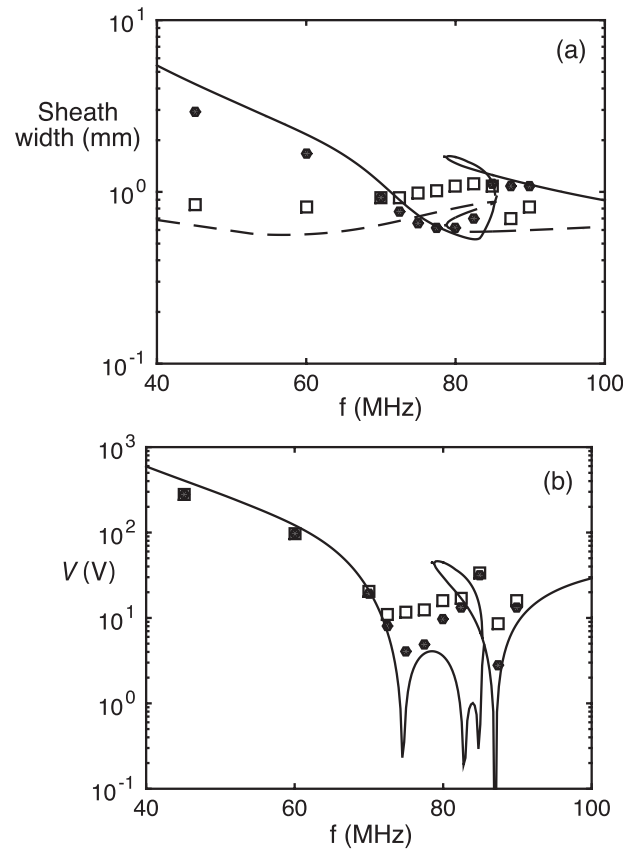

FIG. 8. Comparing the frequency variations for the model with the fluid simulations for $n_e = 2 \times 10^{16}$ m^{-3}; (a) the powered and grounded sheath widths s and w (the lines and symbols give the model and fluid simulation results); (b) the excitation voltage V; the line gives the model results, the symbols give the reactive (dots) and total (open squares) excitation voltage from the fluid simulations.

IV. CONCLUSIONS AND DISCUSSION

Large-area plasma processing systems, capacitively driven at frequencies higher than the conventional frequency of 13.56 MHz, are widely used for silicon wafer and flat panel processing to increase ion flux and reduce ion bombarding energy. At these higher frequencies and larger areas, electromagnetic effects, such as standing waves and skin effects, can limit processing uniformity. To understand these effects in more detail, we developed an analytic discharge model based on the propagation of linear, lossless electromagnetic waves, for a commonly used asymmetrically driven geometry (see Figure 1), with a 15 cm radius powered electrode in a cylindrical discharge 5 cm in height and 25 cm in radius. As in the work of Sansonnens and associates,[7] we considered axially symmetric and axially antisymmetric radially propagating wave modes (see Figure 2). The discharge was modeled as a uniform bulk plasma with a uniform, normally thicker sheath at the smaller area powered electrode and a uniform, normally thinner sheath at the larger area grounded electrode. These were self-consistently determined at a specified plasma density using the Child law to calculate sheath widths and the electron power balance to calculate the rf source voltage. The fields and the system resonant frequencies were then determined, and the center-to-

edge voltage ratio on the powered electrode was calculated versus frequency.

Since the model is analytic, it is computationally efficient, allowing large parameter ranges to be explored. At a pressure of 10 mTorr and a plasma density of $n_e = 1 \times 10^{16}$ m^{-3}, of common industrial interest, we explored a frequency range from 30 to 120 MHz. We found, with increasing frequency, a series of system resonances; the lowest resonance at 61.5 MHz had a mainly antisymmetric character, followed by a mainly symmetric resonance at 88.5 MHz, followed by the next order antisymmetric resonance at 103.55 MHz. We also found an "apparent" resonance of the powered electrode close to the first antisymmetric resonance, which was interpreted in terms of the antisymmetric mode field structure. At a higher density of $n_e = 2 \times 10^{16}$ m^{-3}, we examined a frequency range from 30 to 160 MHz, finding the first four system resonances. The first antisymmetric and symmetric resonances were closer together, and a hysteresis resonance-like behavior appeared between these two resonances. The frequencies of these two resonances were interpreted in terms of the wavenumbers of the first antisymmetric and symmetric modes. The resonance structure gives clearly observable central high sheath voltages on the powered electrode, which are one source of processing nonuniformity. The analytic model results were compared with two-dimensional hybrid fluid-analytical code simulations in a similar asymmetric geometry, in which the powered and grounded electrodes were separated by a 2 cm quartz spacer ring. In addition, the electromagnetic field solve in the simulations includes the power losses, the self-consistent sheath widths in the simulations vary with radius and also exist along the outside conductor at the outer radius of the discharge, and the electron density and temperature also vary within the plasma. Despite these differences, the model and simulation results for the sheath widths, source voltage, and resonance frequencies agreed quite well.

In both the analytic model and the more detailed fluid simulation, energetic electrons and other kinetic effects have not been considered. They would be expected to introduce some additional variation of the results, but probably smaller than those already found between the model and simulations. In any case, the model would not be expected to predict the best operating frequency but rather to indicate the structural changes in the results as the frequency is varied.

In conclusion, a two-dimensional analytic model for a practical asymmetric discharge configuration with unequal sheath widths has been developed, which can be used to examine the resonances for which central highs would affect processing uniformity, and which can be used to examine the uniformity as the operating frequency is varied.

ACKNOWLEDGMENTS

APPENDIX A: ELECTRIC FIELDS

The E_r fields in region 1 are found by substituting expressions (9)–(11) into (5)

$$E_{r1} = \frac{1}{j\omega\epsilon_0} \Big[A_{s1}\beta_{s1} \operatorname{sech}\beta_{s1}w \cosh\alpha_{s1}(d+\delta_{s1})\sinh\beta_{s1}(l-z)\,\mathrm{J}_1(k_{s1}r) \\ + A_{a1}\beta_{a1} \operatorname{sech}\beta_{a1}w \sinh\alpha_{a1}(d+\delta_{a1})\sinh\beta_{a1}(l-z)\,\mathrm{J}_1(k_{a1}r) \Big], \quad d < z < l, \tag{A1}$$

$$E_{r1} = -\frac{1}{j\omega\epsilon_0\kappa_p} \Big[A_{s1}\alpha_{s1} \sinh\alpha_{s1}(z+\delta_{s1})\,\mathrm{J}_1(k_{s1}r) + A_{a1}\alpha_{a1} \cosh\alpha_{a1}(z+\delta_{a1})\,\mathrm{J}_1(k_{a1}r) \Big], \quad -h < z < d, \tag{A2}$$

$$E_{r1} = -\frac{1}{j\omega\epsilon_0} \Big[A_{s1}\beta_{s1} \operatorname{sech}\beta_{s1}s \cosh\alpha_{s1}(h-\delta_{s1})\sinh\beta_{s1}(l+z)\,\mathrm{J}_1(k_{s1}r) \\ - A_{a1}\beta_{a1} \operatorname{sech}\beta_{a1}s \sinh\alpha_{a1}(h-\delta_{a1})\sinh\beta_{a1}(l+z)\,\mathrm{J}_1(k_{a1}r) \Big], \quad -l < z < -h. \tag{A3}$$

The E_z fields are similarly obtained by substituting expressions (9)–(11) into (6)

$$E_{z1} = \frac{1}{j\omega\epsilon_0} \Big[A_{s1}k_{s1} \operatorname{sech}\beta_{s1}w \cosh\alpha_{s1}(d+\delta_{s1})\cosh\beta_{s1}(l-z)\,\mathrm{J}_0(k_{s1}r) \\ + A_{a1}k_{a1} \operatorname{sech}\beta_{a1}w \sinh\alpha_{a1}(d+\delta_{a1})\cosh\beta_{a1}(l-z)\,\mathrm{J}_0(k_{a1}r) \Big], \quad d < z < l, \tag{A4}$$

$$E_{z1} = -\frac{1}{j\omega\epsilon_0\kappa_p} \Big[A_{s1}k_{s1} \cosh\alpha_{s1}(z+\delta_{s1})\,\mathrm{J}_0(k_{s1}r) + A_{a1}k_{a1} \sinh\alpha_{a1}(z+\delta_{a1})\,\mathrm{J}_0(k_{a1}r) \Big], \quad -h < z < d, \tag{A5}$$

$$E_{z1} = \frac{1}{j\omega\epsilon_0} \Big[A_{s1}k_{s1} \operatorname{sech}\beta_{s1}s \cosh\alpha_{s1}(h-\delta_{s1})\cosh\beta_{s1}(l+z)\,\mathrm{J}_0(k_{s1}r) \\ - A_{a1}k_{a1} \operatorname{sech}\beta_{a1}s \sinh\alpha_{a1}(h-\delta_{a1})\cosh\beta_{a1}(l+z)\,\mathrm{J}_0(k_{a1}r) \Big], \quad -l < z < -h. \tag{A6}$$

The E_r fields in region 2 are found by substituting expressions (19)–(21) into (5)

$$E_{r2} = \frac{1}{j\omega\epsilon_0}\left[A_{s2}\beta_{s2}\,\text{sech}\,\beta_{s2}w\cosh\alpha_{s2}d\sinh\beta_{s2}(l-z)\,(\text{J}_1(k_{s2}r)+b_{s2}\text{N}_1(k_{s2}r))\right.$$
$$\left.+A_{a2}\beta_{a2}\,\text{sech}\,\beta_{a2}w\sinh\alpha_{a2}d\sinh\beta_{a2}(l-z)\,(\text{J}_1(k_{a2}r)+b_{a2}\text{N}_1(k_{a2}r))\right], \qquad d < z < l, \tag{A7}$$

$$E_{r2} = -\frac{1}{j\omega\epsilon_0\kappa_p}\left[A_{s2}\alpha_{s2}\sinh\alpha_{s2}z\,(\text{J}_1(k_{s2}r)+b_{s2}\text{N}_1(k_{s2}r))+A_{a2}\alpha_{a2}\cosh\alpha_{a2}z\,(\text{J}_1(k_{a2}r)+b_{a2}\text{N}_1(k_{a2}r))\right], \quad -d < z < d, \tag{A8}$$

$$E_{r2} = -\frac{1}{j\omega\epsilon_0}\left[A_{s2}\beta_{s2}\,\text{sech}\,\beta_{s2}w\cosh\alpha_{s2}d\sinh\beta_{s2}(l+z)\,(\text{J}_1(k_{s2}r)+b_{s2}\text{N}_1(k_{s2}r))\right.$$
$$\left.-A_{a2}\beta_{a2}\,\text{sech}\,\beta_{a2}w\sinh\alpha_{a2}d\sinh\beta_{a2}(l+z)\,(\text{J}_1(k_{a2}r)+b_{a2}\text{N}_1(k_{a2}r))\right], \qquad -l < z < -d. \tag{A9}$$

The E_z fields are similarly obtained by substituting expressions (19)–(21) into (6)

$$E_{z2} = \frac{1}{j\omega\epsilon_0}\left[A_{s2}k_{s2}\,\text{sech}\,\beta_{s2}w\cosh\alpha_{s2}d\cosh\beta_{s2}(l-z)\,(\text{J}_0(k_{s2}r)+b_{s2}\text{N}_0(k_{s2}r))\right.$$
$$\left.+A_{a2}k_{a2}\,\text{sech}\,\beta_{a2}w\sinh\alpha_{a2}d\cosh\beta_{a2}(l-z)\,(\text{J}_0(k_{a2}r)+b_{a2}\text{N}_0(k_{a2}r))\right], \qquad d < z < l, \tag{A10}$$

$$E_{z2} = -\frac{1}{j\omega\epsilon_0\kappa_p}\left[A_{s2}k_{s2}\cosh\alpha_{s2}z\,(\text{J}_0(k_{s2}r)+b_{s2}\text{N}_0(k_{s2}r))\right.$$
$$\left.+A_{a2}k_{a2}\sinh\alpha_{a2}z\,(\text{J}_0(k_{a2}r)+b_{a2}\text{N}_0(k_{a2}r))\right], \qquad -d < z < d, \tag{A11}$$

$$E_{z2} = \frac{1}{j\omega\epsilon_0}\left[A_{s2}k_{s2}\,\text{sech}\,\beta_{s2}w\cosh\alpha_{s2}d\cosh\beta_{s2}(l+z)\,(\text{J}_0(k_{s2}r)+b_{s2}\text{N}_0(k_{s2}r))\right.$$
$$\left.-A_{a2}k_{a2}\,\text{sech}\,\beta_{a2}w\sinh\alpha_{a2}d\cosh\beta_{a2}(l+z)\,(\text{J}_0(k_{a2}r)+b_{a2}\text{N}_0(k_{a2}r))\right], \qquad -l < z < -d. \tag{A12}$$

APPENDIX B: APPROXIMATE EIGENVALUES

For a low density plasma with a skin depth $c/\omega_p \gg l$, we can take $\tanh(x) \to x$ and $\coth(x) \to 1/x$ in (14)–(17) to obtain the approximate solutions in region 1

$$\delta_{s1} \approx -l\frac{s-w}{s+w}, \tag{B1}$$

$$k_{s1}^2 \approx k_0^2\frac{2l}{s+w}, \tag{B2}$$

$$\beta_{s1}^2 \approx k_{s1}^2 - k_0^2, \tag{B3}$$

$$\alpha_{s1}^2 \approx -k_0^2\kappa_p, \tag{B4}$$

$$\delta_{a1} \approx l\frac{s-w}{s+w}+w-s, \tag{B5}$$

$$k_{a1}^2 \approx k_0^2 - \frac{s+w}{\kappa_p sw(h+d)}, \tag{B6}$$

$$\beta_{a1}^2 \approx k_{a1}^2 - k_0^2, \tag{B7}$$

$$\alpha_{a1}^2 \approx k_{a1}^2 - k_0^2\kappa_p. \tag{B8}$$

In region 2, the approximate solutions are[7]

$$k_{s2}^2 \approx k_0^2\frac{l}{w}, \tag{B9}$$

$$\beta_{s2}^2 \approx k_{s2}^2 - k_0^2, \tag{B10}$$

$$\alpha_{s2}^2 \approx -k_0^2\kappa_p, \tag{B11}$$

$$k_{a2}^2 \approx k_0^2 - \frac{1}{\kappa_p wd}, \tag{B12}$$

$$\beta_{a2}^2 \approx k_{a2}^2 - k_0^2, \tag{B13}$$

$$\alpha_{a2}^2 \approx k_{a2}^2 - k_0^2\kappa_p. \tag{B14}$$

APPENDIX C: SOLUTION PROCEDURE

For a given electron density, at each frequency, the electromagnetics and the nonlinear Child laws and electron power balance are simultaneously solved by a two-dimensional root-finding procedure as follows: For an initial guess $(s^{(0)}, w^{(0)})$ of the sheath widths, the linear electromagnetics system (33) is solved for a unit voltage excitation $(V \equiv 1)$, and the average sheath voltages $\hat{V}_s$ and $\hat{V}_w$ at the powered and grounded electrodes, and the stochastic and ohmic heating powers $\hat{P}_{\text{stoc}}$ and $\hat{P}_{\text{ohm}}$, are evaluated (here "hat" denotes the voltages and powers for a unit voltage excitation). Using (37) and (38) in the power balance relation $P_{e,\text{lost}} = P_{e,\text{abs}}$, we then obtain

$$P_{e,\text{lost}} = \hat{P}_{\text{stoc}}V + \hat{P}_{\text{ohm}}V^2, \tag{C1}$$

which is solved to determine the source voltage $V^{(0)}$. The Child laws (34) and (35) are then used to determine corrected values of the sheath widths

$$s^{(1)} = \frac{K_{\text{CL}}\left(\hat{V}_s V^{(0)}\right)^{3/4}}{1.23} + 2.61\,\lambda_D, \tag{C2}$$

$$w^{(1)} = \frac{K_{\text{CL}}\left(\hat{V}_w V^{(0)}\right)^{3/4}}{1.23} + 2.61\,\lambda_D. \tag{C3}$$

The Matlab root solver `fsolve` is used to obtain converged values of the sheath widths. Logarithmic variables are actually used ($\ln s$ and $\ln w$), so that the root solver searches only over positive values of the sheath widths.

[1]M. A. Lieberman and A. J. Lichtenberg, *Principles of Plasma Discharges and Materials Processing*, 2nd ed. (Wiley, 2005).

[2]T. Makabe and Z. L. Petrovic, *Plasma Electronics: Applications in Microelectronic Device Fabrication* (Taylor and Francis Ltd., 2006).

[3]P. Chabert and N. Braithwaite, *Physics of Radiofrequency Plasmas* (Cambridge University Press, 2011).

[4]L. Sansonnens and J. Schmitt, Appl. Phys. Lett. **82**, 182 (2003).

[5]A. Perret, P. Chabert, J. P. Booth, J. Jolly, J. Guillon, and Ph. Auvray, Appl. Phys. Lett. **83**, 243 (2003).

[6]M. A. Lieberman, J. P. Booth, P. Chabert, J. M. Rax, and M. M. Turner, Plasma Sources Sci. Technol. **11**, 283 (2002).

[7]L. Sansonnens, A. A. Howling, and Ch. Hollenstein, Plasma Sources Sci. Technol. **15**, 302 (2006).

[8]P. Chabert, J. L. Raimbault, J. M. Rax, and M. A. Lieberman, Phys. Plasmas **11**, 1775 (2004).

[9]P. Chabert, J. L. Raimbault, J. M. Rax, and A. Perret, Phys. Plasmas **11**, 4081 (2004).

[10]P. Chabert, J. L. Raimbault, P. Levif, J. M. Rax, and M. A. Lieberman, Phys. Rev. Lett. **95**, 205001 (2005).

[11]P. Chabert, J. L. Raimbault, P. Levif, J. M. Rax, and M. A. Lieberman, Plasma Sources Sci. Technol. **15**, S130 (2006).

[12]P. Chabert, J. Phys. D: Appl. Phys. **40**, R63 (2007).

[13]I. Lee, M. A. Lieberman, and D. B. Graves, Plasma Sources Sci. Technol. **17**, 015018 (2008).

[14]S. Rauf, K. Bera, and K. Collins, Plasma Sources Sci. Technol. **17**, 035003 (2008).

[15]E. Kawamura, D. B. Graves, and M. A. Lieberman, Plasma Sources Sci. Technol. **20**, 035009 (2011).

[16]E. Kawamura, M. Lieberman, and D. B. Graves, Plasma Sources Sci. Technol. **23**, 064003 (2014).

[17]Y. Yang and M. J. Kushner, Plasma Sources Sci. Technol. **19**, 055011 (2010).

[18]Y. Yang and M. J. Kushner, Plasma Sources Sci. Technol. **19**, 055012 (2010).

[19]Y. R. Zhang, S. X. Zhao, A. Bogaerts, and Y. N. Wang, Phys. Plasmas **17**, 113512 (2010).

[20]Z. Chen, S. Rauf, and K. Collins, J. Appl. Phys. **108**, 073301 (2010).

[21]S. Rauf, Z. Chen, and K. Collins, J. Appl. Phys. **107**, 093302 (2010).

[22]D. Eremin, T. Hemke, R. P. Brinkmann, and T. Mussenbrock, J. Phys. D: Appl. Phys. **46**, 084017 (2013).

[23]M. A. Lieberman, A. J. Lichtenberg, and E. Kawamura, Plasma Sources Sci. Technol. **24**, 055011 (2015).

[24]J. P. M. Schmitt, Thin Solid Films **174**, 193 (1989).

[25]L. Sansonnens, A. Pletzer, D. Magni, A. A. Howling, Ch. Hollenstein, and J. P. M. Schmitt, Plasma Sources Sci. Technol. **6**, 170 (1997).

[26]J. P. M. Schmitt, M. Elyaakoubi, and L. Sansonnens, Plasma Sources Sci. Technol. **11**, A206 (2002).

[27]H. Schmidt, L. Sansonnens, A. A. Howling, Ch. Hollenstein, L. Derendinger, M. Elyaakoubi, and J. P. M. Schmitt, J. Appl. Phys. **95**, 4559 (2004).

[28]L. Sansonnens, J. Appl. Phys. **97**, 063304 (2005).

[29]A. A. Howling, L. Sansonnens, L. Ballutaud, Ch. Hollenstein, and J. P. M. Schmitt, J. Appl. Phys. **96**, 5429 (2004).

[30]A. A. Howling, L. Derendinger, L. Sansonnens, H. Schmidt, Ch. Hollenstein, E. Sakanaka, and J. P. M. Schmitt, J. Appl. Phys. **97**, 123308 (2005).

[31]L. Sansonnens, B. Strahm, L. Derendinger, A. A. Howling, Ch. Hollenstein, E. Sakanaka, Ch. Ellert, and J. P. M. Schmitt, J. Vac. Sci. Technol., A **23**, 922 (2005).

[32]A. A. Howling, L. Sansonnens, H. Schmidt, and Ch. Hollenstein, Appl. Phys. Lett. **87**, 076101 (2005).

[33]E. Kawamura, A. J. Lichtenberg, M. A. Lieberman, and A. M. Marakhtanov, "2D fluid-analytical simulation of electromagnetic effects in low pressure, high frequency electronegative capacitive discharges," Plasma Sources Science and Technology (submitted).